Monthly Notices
of the
ROYAL ASTRONOMICAL SOCIETY

MNRAS **469,** L123–L127 (2017)
Advance Access publication 2017 May 1

doi:10.1093/mnrasl/slx067

ALMA polarization observations of the particle accelerators in the hotspot of the radio galaxy 3C 445

M. Orienti,[1]★ G. Brunetti,[1] H. Nagai,[2] R. Paladino,[1] K.-H. Mack[1] and M. A. Prieto[3]

[1]*INAF – Istituto di Radioastronomia, via Gobetti 101, I-40129 Bologna, Italy*
[2]*National Astronomical Observatory of Japan, Osawa 2-21-1, Mitaka, Tokyo 181-8588, Japan*
[3]*Instituto de Astrofísica de Canarias (IAC), E-38200 La Laguna, Tenerife, Spain*

Accepted 2017 April 27. Received 2017 April 27; in original form 2017 February 28

ABSTRACT

We present Atacama Large Millimeter Array polarization observations at 97.5 GHz of the southern hotspot of the radio galaxy 3C 445. The hotspot structure is dominated by two bright components enshrouded by diffuse emission. Both components show fractional polarization between 30 and 40 per cent, suggesting the presence of shocks. The polarized emission of the western component has a displacement of about 0.5 kpc outward with respect to the total intensity emission and may trace the surface of a front shock. Strong polarization is observed in a thin strip marking the ridge of the hotspot structure visible from radio to optical. No significant polarization is detected in the diffuse emission between the main components, suggesting a highly disordered magnetic field likely produced by turbulence and instabilities in the downstream region that may be at the origin of the extended optical emission observed in this hotspot. The polarization properties support a scenario in which a combination of both multiple and intermittent shock fronts due to jet dithering and spatially distributed stochastic second-order Fermi acceleration processes are present in the hotspot complex.

Key words: acceleration of particles – polarization – radiation mechanisms: non-thermal – radio continuum: galaxies.

1 INTRODUCTION

Radio hotspots are bright and compact regions located at the edges of powerful Fanaroff-Riley type II (FRII) radio galaxies (Fanaroff & Riley 1974). In the standard scenario, hotspots are considered to be the working surfaces of the supersonic jets launched by the active galactic nucleus which impact on the surrounding ambient medium. In these regions a shock is produced, leading to the acceleration of relativistic particles transported by the jet and enhancing their emission. This scenario predicts very efficient particle acceleration and has been strongly supported by the detection of synchrotron optical/infrared emission from a number of hotspots (e.g. Meisenheimer, Yates & Röser 1997; Cheung, Wardle & Chen 2004; Mack et al. 2009).

In the standard shock model, particle acceleration occurs very locally, implying that optical emission should arise from a very compact region, up to a few hundred parsecs in size, due to the short radiative lifetime of the energetic electrons ($\gamma > 10^5$). This simple shock scenario has been challenged by the discovery of kpc-scale extended optical emission in a handful of hotspots, like 3C 445 South (Prieto, Brunetti & Mack 2002), 3C 105 South (Orienti et al. 2012), 3C 445 North, 3C 227 West (Mack et al. 2009), Pictor A (Thomson, Crane & MacKay 1995), 3C 33, 3C 111, 3C 303, 3C 351 (Lähteenmäki & Valtaoja 1999), 3C 390.3 (Prieto & Kotilainen 1997), 3C 275.1 (Cheung et al. 2004) and 4C 74.26 (Erlund et al. 2010).

The discovery of kpc-scale diffuse optical emission suggests that additional efficient and spatially distributed acceleration mechanisms must take place in order to compensate the radiative losses and to explain the extended synchrotron optical emission. The nature of this additional acceleration process is still unclear. It may be either multiple/complex shock surfaces in the hotspot region or efficient spatially distributed second-order acceleration processes driven by turbulence in the downstream region. The latter hypothesis was proposed in the case of the hotspot 3C 445 South (Prieto et al. 2002).

The peculiar hotspot 3C 445 South is clearly detected from radio to X-rays (Perlman et al. 2010; Orienti et al. 2012). This hotspot has an east–west arc-shaped structure of about 10 × 3 kpc in size with two main compact components enshrouded by diffuse emission visible in radio, NIR and optical bands. In the optical, another compact component is present to the north-west of the brightest radio component (Orienti et al. 2012). Its location is marked as North in Fig. 1. The X-ray emission is misaligned with respect to the two main components and is more consistent with the position of the compact

★ E-mail: orienti@ira.inaf.it

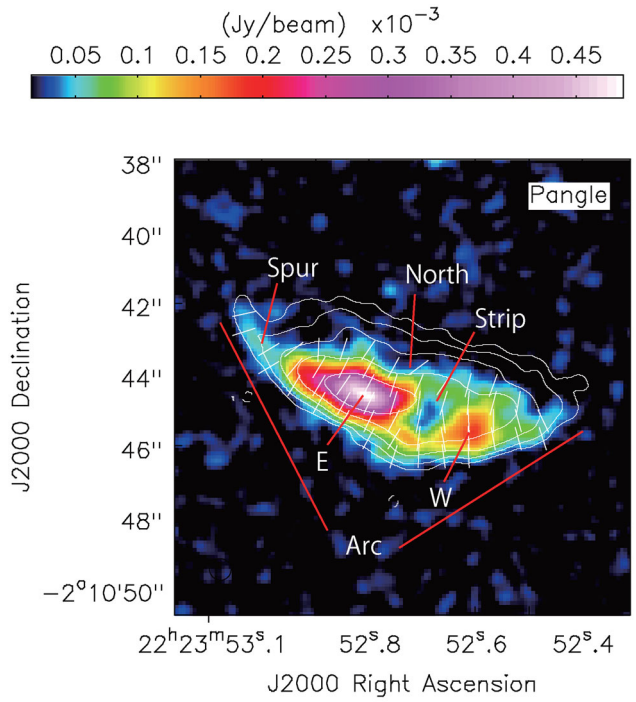

Figure 1. ALMA image at 97.5 GHz of 3C 445 South in total intensity (contours) overlaid on polarization intensity (colour-scale). The total intensity peak flux density is 1.3 mJy beam^{-1}. The first contour is 45 μJy, which is three times the rms measured on the total intensity image. Contours increase by a factor of 2. The polarization intensity colour scale is shown by the wedge at the top of the image. The 1-σ noise level measured on the polarization image plane is 12 μJy beam^{-1}. Vectors represent the electric vector position angle. The restoring beam is plotted on the bottom left corner.

optical component (Perlman et al. 2010; Orienti et al. 2012). Prieto et al. (2002) suggested that the development of instabilities in the cocoon may produce magneto-hydrodynamic turbulence that can account for the spatially distributed reacceleration of the relativistic electrons that is required to explain the diffuse optical emission between the compact components. Such a second-order acceleration mechanism becomes efficient in the presence of a low magnetic field (a few tens of milliGauss), as the one estimated for 3C 445 South (Prieto et al. 2002). However, a clear evidence in support of either the multiple/complex shock scenario or the turbulence model requires deep polarimetric observations in the millimeter regime where contributions from the steep-spectrum lobe and from the Faraday rotation are marginal. Alfvénic or super-Alfvénic turbulence is expected to tangle efficiently the magnetic field on multiple scales and thus to reduce significantly the fractional polarization.

In this Letter, we present results on Atacama Large Millimeter Array (ALMA) full-polarization observations at 97.5 GHz (3 mm) of the hotspot 3C 445 South. The polarization properties provide us with information on the ordered component of the magnetic field and its topology in the hotspot region. ALMA data are then complemented with Very Large Array (*VLA*) observations at 8.4 GHz in order to trace the spectral index distribution.

This Letter is organized as follows: in Section 2, we describe the observation and data reduction. In Section 3, we present results on the ALMA data analysis and in Section 4, we discuss the polarization and spectral index properties in the context of particle acceleration processes.

Throughout this Letter, we assume the following cosmology: $H_0 = 71$ km s^{-1} Mpc^{-1}, $\Omega_M = 0.27$ and $\Omega_\Lambda = 0.73$, in a flat universe. At the redshift of the target, $z = 0.0558$, the luminosity distance D_L is 252 Mpc, and 1 arcsec = 1.09 kpc.

2 OBSERVATIONS AND DATA REDUCTION

We observed the hotspot 3C 445 South with ALMA during Cycle 2 using the Band 3 receiver (97.5 GHz) in full polarization (project ID: #2013.1.00286.S). The observations were performed on 2015 September 3 and 32 good antennas participated in the observing run. The target on-source observing time was 2 h, for a total observing time of 3 h that was required for ensuring a sufficient parallactic angle coverage. 3C 446 was observed as the bandpass and phase calibrator, while Ceres was observed as the flux calibrator. However, it has been found out that Ceres gives an inaccurate flux calibration, so the phase calibrator has been used instead, taking the flux from the ALMA catalogue (1.322 Jy at 97.5 GHz). In addition, J2134-0153 was observed for calibration of the instrumental polarization (D-terms), cross-hand delay and cross-hand phase.

Calibration and data reduction were done using Common Astronomical Software Applications (CASA) version 4.7.0. Details of ALMA polarization data calibration can be found in Nagai et al. (2016). Final images have an rms of 15 μJy beam^{-1} in Stokes I, and 12 μJy beam^{-1} in Stokes Q and U. The resolution is 0.6 arcsec. No primary beam correction was needed since the target was on-axis. Images in Stokes Q and U have been used to produce the polarization intensity and polarization angle images (Fig. 1), as well as the fractional polarization image and the associated statistical error image (Fig. 2). Blanking on the fractional polarization image was done by clipping the pixels of the total intensity image with values below three times the rms measured on the off-source image plane.

In addition to the ALMA data, we made use of *VLA* observations at 8.4 GHz in A-configuration to perform the spectral index analysis. Calibration and data reduction of *VLA* data can be found in Orienti et al. (2012). We produced another set of *VLA* and ALMA images with the same *uv*-range, resolution and image sampling. Image registration was carried out by comparing the peak of the brightest optically thin hotspot component. Then, we produced a spectral index image[1] between 97.5 and 8.4 GHz. Blanking was done by clipping the pixels of the input images with values below three times the rms measured on the off-source image plane at each frequency (Fig. 3). Despite the particular care used to produce and align the images, some gradients at the edges are visible due to the slightly larger extension of the hotspot complex at the lower frequency.

The total intensity flux density at 8.4 and at 97.5 GHz and the polarization flux density at 97.5 GHz are extracted from the same region by selecting polygonal areas. The values are reported in Table 1. Spectral index errors are computed by assuming a 3 per cent uncertainty on the amplitude scale at both frequencies and considering the error propagation theory. Errors on the polarization parameters were computed following Fanti et al. (2004) and range from about 0.5 per cent in the brightest regions up to 25−50 per cent in the ridge of the hotspot structure with low signal-to-noise ratio (SNR) (see Section 3).

[1] In this Letter, we define the spectral index α as $S_\nu \propto \nu^{-\alpha}$.

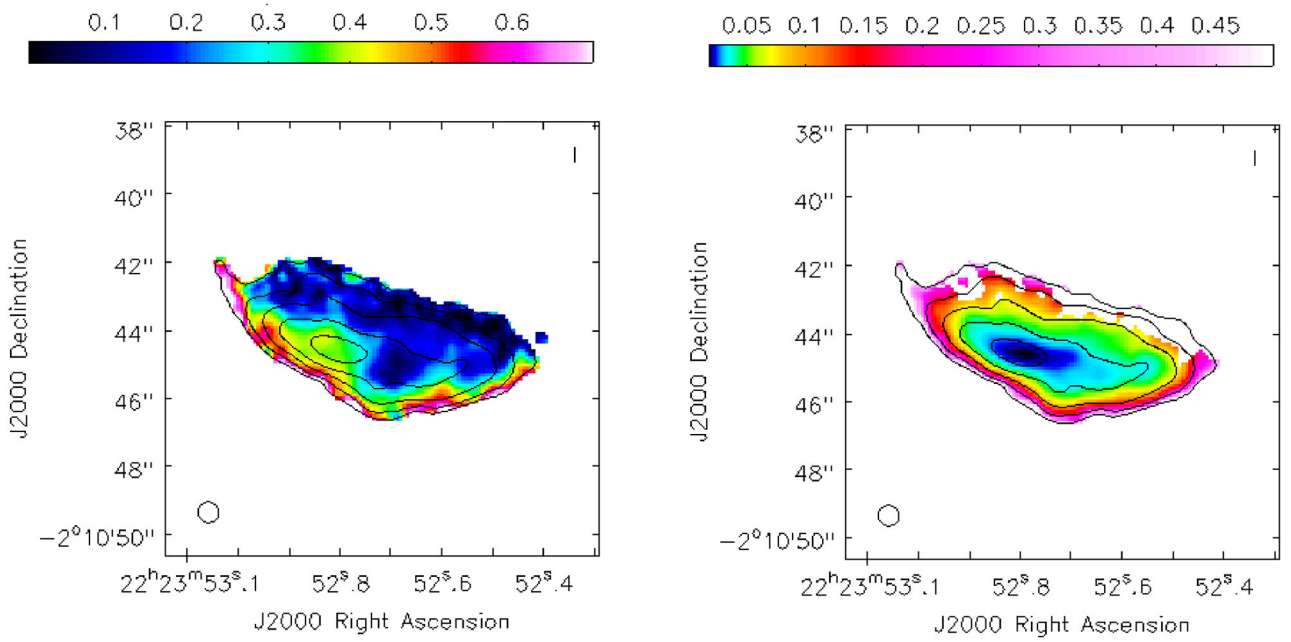

Figure 2. ALMA image at 97.5 GHz of 3C 445 South in total intensity (contours) overlaid on the fractional polarization (left-hand panel) and fractional polarization error (right-hand panel) images (colour-scale). The total intensity peak flux density is 1.3 mJy beam^{-1}. The first contour is 45 μJy, which is three times the rms measured on the total intensity image. Contours increase by a factor of 2. The fractional polarization and the fractional polarization error colour scales are shown by the wedge at the top of the images. The restoring beam is plotted on the bottom left corner.

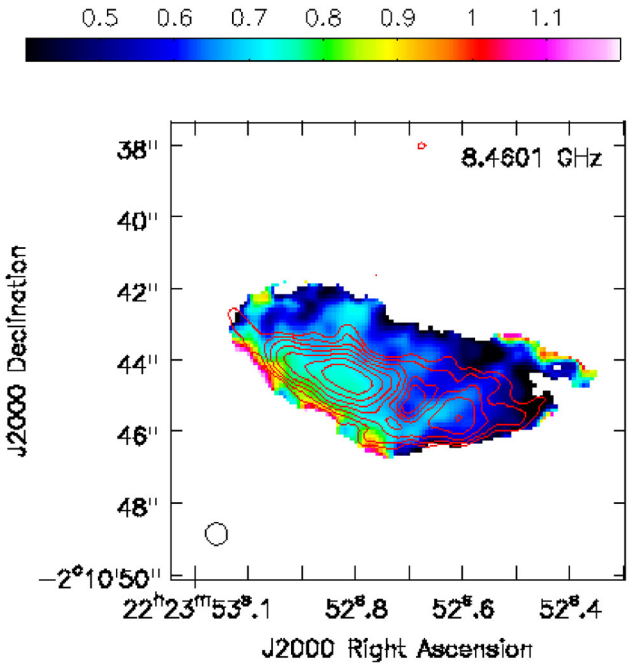

Figure 3. Colour-scale spectral index image between 97.5 and 8.4 GHz of 3C 445 South superimposed on the ALMA polarization image at 97.5 GHz (contours). The first contour is 45 μJy beam^{-1}, which corresponds to three times the rms measured on the image plane. Contour levels increase by a factor of $\sqrt{2}$. The colour scale is shown by the wedge at the top of the image. The restoring beam is plotted on the bottom left corner.

3 RESULTS

In the ALMA image at 97.5 GHz, the hotspot 3C 445 South shows an elongated structure with two main components (labelled W and E in Fig. 1) enshrouded by diffuse emission, in good agreement with what was already found at cm-wavelengths and in NIR/optical bands (Orienti et al. 2012). The polarization percentage of the whole hotspot is about 27 per cent. Although the percentage integrated over the main components is about 30 per cent, it may reach peak values as high as 40 and 35 per cent in the E and W component, respectively (Fig. 1). Polarized emission is observed along the ridge of the arc-shaped structure, with a polarization percentage from about 30 per cent up to 70 per cent in the north-eastern spur (Fig. 1 and left-hand panel of Fig. 2). The uncertainty on the fractional polarization depends on the SNR and is smaller for higher SNR (right-hand panel of Fig. 2). The electric vector position angles (EVPA) range between -33° and -22° in the E component and between -5° and 15° in the W component (Fig. 1). There is a clear offset of about 0.5 arcsec (0.5 kpc) between the peak of the total intensity and the peak of polarized emission of the W component, in the sense that the total intensity is nearer the nucleus.

A strip of polarized emission of about 15 per cent is detected to the north of the two main components (Figs 1 and 2). The compact component detected in optical/X-ray bands (labelled North in Fig. 1) is located in this polarized region. No significant polarization is observed from the diffuse emission ($<3\,\sigma$). In particular, between E and W, we could set a tight upper limit on the fractional polarization of about 4 per cent, which corresponds to the fractional polarization error computed in that region (Fig. 2).

The spectral index between 97.5 and 8.4 GHz integrated over the whole hotspot is $\alpha = 0.64 \pm 0.02$ and is derived from the set of images with the same *uv*-range, resolution and sampling at both frequencies. The spectral index of the E and W components is $\alpha = 0.70 \pm 0.02$ and 0.62 ± 0.02, respectively. The spectral index of the diffuse emission ranges between 0.55 and 0.65. It is interesting to notice that between E and W, where no significant polarization is detected, the spectral index is 0.60 ± 0.02, and thus is slightly flatter than in the two compact and highly polarized components.

Table 1. Observational parameters of the hotspot 3C 445 South. Column 1: hotspot component. Columns 2 and 3: total intensity flux density at 8.4 and 97.5 GHz, respectively. Column 4: polarization flux density. Column 5: polarization percentage. Column 6: spectral index between 97.5 and 8.4 GHz.

Comp.	$S_{8.4}$ (mJy)	$S_{97.5}$ (mJy)	p (mJy)	m (per cent)	α
E	44.5 ± 1.3	7.86 ± 0.24	2.50 ± 0.08	32	0.70 ± 0.02
W	14.4 ± 0.5	3.15 ± 0.09	0.90 ± 0.03	29	0.62 ± 0.02
Tot	99.3 ± 3.0	20.4 ± 0.61	5.61 ± 0.17	27	0.64 ± 0.02

4 DISCUSSION AND CONCLUSIONS

Synchrotron optical emission extending on kpc-scale is hard to reconcile with the short radiative time of energetic optical-emitting electrons and indicates the presence of *in situ* reacceleration processes. The nature of these acceleration mechanisms, either Fermi-I processes like shocks or stochastic Fermi-II processes, is still unclear. Prieto et al. (2002) proposed a scenario in which electrons are first reaccelerated in a single region by strong shocks (Fermi-I) and then, after being released from the shock region, are transported to the cocoon where they are further reaccelerated by turbulence and compression. The diffuse optical emission and the secondary W component were then explained by means of stochastic Fermi-II mechanisms that become efficient in presence of low magnetic fields ($\lesssim$100 μG) that prevent fast particle cooling, like in the case of the low-luminosity hotspot of 3C 445 (Prieto et al. 2002; Brunetti et al. 2003).

ALMA observations in the millimeter regime detect a high fraction of polarized emission from various structures of the hotspot complex. In both E and W components the fractional polarization reaches values of about 35–40 per cent. A polarization percentage between 30 and 70 per cent is observed along the ridge of the 12-kpc arc-shaped structure, although the low SNR prevents a tight constraint of its value. Additional polarization of about 15 per cent is also observed in the northern strip bridging the E and W components (Fig. 2).

These polarization percentages are too high to be reconciled with a turbulent and uncompressed magnetic field. Conversely they indicate the presence of multiple shock regions where the field is compressed in the direction perpendicular to the shock fronts, one of them being coincident with component W. Following Laing (1980), such high degrees of polarization may be observed when our line of sight is roughly parallel to the compression front and thus forms a large angle to the jet axis ($\gtrsim$60°). In this case, it is unlikely that the X-ray emission is produced by inverse Compton scattering of Cosmic Microwave Background photons in a decelerating jet (e.g. Georganopoulos & Kazanas 2004). This supports the synchrotron radiation as the origin of the X-ray emission. The EVPA are perpendicular to the highly polarized structures, in agreement with what was found by Leahy et al. (1997) at 8.4 GHz, further supporting the presence of strong shocks. It is worth mentioning that the peak of the polarized emission occurs about 0.5 kpc from the peak of the total intensity, in a region where the spectrum is slightly flatter ($\alpha \sim 0.63$) than the spectral index measured in the region of the total intensity peak ($\alpha \sim 0.69$). This result is in agreement with the idea that the polarization marks the shock front, while the total intensity emission traces also backflow material.

The large-scale shock surface traced by the polarization marks the largest scales where the kinetic energy of the jet is dissipated. The multiple shock surfaces (i.e. the E and W components imaged from radio to optical band, as well as the North component detected in the optical) suggest either that the jet may change its direction, creating a dentist drill effect, or that the shock surface is very complicated. Changes in the jet directions may be caused by instabilities as the jet interacts with backflow material (e.g. Perucho et al. 2014; Tchekhovskoy & Bromberg 2016). In principle, shocks would accelerate electrons to very high energies and this has been used to highlight some tension between shock acceleration models and the optical synchrotron cut-off observed in some hotspots (Araudo et al. 2016). Given our results, this tension may be circumvent by assuming that the shock acceleration occurs in an intermittent way. It is possible that the E and W components mark regions where particle acceleration occurred 100–1000 yr ago while the North component that emerges in the optical band and that is probably emitting synchrotron radiation up to X-rays pinpoints acceleration that is taking place at the current epoch. A similar scenario has been proposed for explaining the X-ray emission in the hotspot of Pictor A. Tingay et al. (2008) suggested that X-rays in Pictor A are produced by synchrotron emission from compact pc-scale transient regions of enhanced magnetic field. This is consistent also with the recent discovery of temporal variability of the X-ray emission in the hotspot of Pictor A (Hardcastle et al. 2016).

An important result obtained by our ALMA observations of the hotspot 3C 445 South is the lack of significant polarization between E and W and in the diffuse emission located to the north of the polarized emission and visible up to the optical *I*-, *R*- and *B*-band (Orienti et al. 2012). Due to the lack of polarization, the magnetic field in this region should be tangled on scales that are much smaller than the beam equivalent scale, i.e. 600 pc. Specifically, assuming a simple picture where the turbulent magnetic field produces random polarization orientation, the size of the turbulent cells should be

$$l_{\rm t} \sim \left(\frac{p_{\rm obs}}{p_{\rm int}}\right)^{2/3} \left(\frac{A_{\rm b}}{0.3\ {\rm kpc}^2}\frac{\phi}{4\ {\rm kpc}}\right)^{1/3} {\rm kpc} \quad (1)$$

where $p_{\rm obs}$ and $p_{\rm int}$ are the observed and intrinsic polarization percentages, respectively, $A_{\rm b}$ is the beam area and ϕ is the size of the turbulent region. If in equation (1) we consider $p_{\rm int} \sim 70$ per cent and $p_{\rm obs} < 4$ per cent, we obtain $l_{\rm t} \sim 160$ pc. Particles injected in E and W are then transported and possibly reaccelerated downstream in a turbulent magnetic field by Fermi-II mechanisms.[2] The spectrum of the diffuse emission, which is flatter than in the main shock fronts, may support this interpretation.

In the hotspot of 3C 445, the detection of strong shocks occurring in different regions, as well as efficient stochastic Fermi-II processes taking place in the diffuse emission, clearly indicates a complex distribution and nature of particle acceleration at the edge of radio galaxies. Furthermore, it provides a significant modification to the classical scenario of shock acceleration that is routinely adopted for hotspots.

[2] The scale derived from polarization is in line with the turbulence scales, ∼20 pc, that were derived by Prieto et al. (2002) to explain optical emission via Fermi-II acceleration.

Further, high-frequency full-polarization observations of hotspots with diffuse optical emission will be useful for determining the incidence of the various acceleration mechanisms and their distribution across the hotspot structure.

ACKNOWLEDGEMENTS

This Letter makes use of the following ALMA data: ADS/JAO. ALMA#2013.1.00286.S. ALMA is a partnership of ESO (representing its member states), NSF (USA) and NINS (Japan), together with NRC (Canada), NSC and ASIAA (Taiwan), and KASI (Republic of Korea), in cooperation with the Republic of Chile. The Joint ALMA Observatory is operated by ESO, AUI/NRAO and NAOJ. The *VLA* is operated by the US National Radio Astronomy Observatory, which is a facility of the National Science Foundation operated under cooperative agreement by Associated Universities, Inc. Part of this work was done with the contribution of the Italian Ministry of Foreign Affairs and Research for the collaboration project between Italy and Japan. HN is supported by MEXT KAKENHI grant number 15K17619.

REFERENCES

Araudo A. T., Bell A. R., Crilly A., Blundell K. M., 2016, MNRAS, 460, 3554
Brunetti G., Mack K.-H., Prieto M. A., Varano S., 2003, MNRAS, 345, 40
Cheung C. C., Wardle J. F. C., Chen T., 2005, ApJ, 628, 104
Erlund M. C., Fabian A. C., Blundell K. M., Crawford C. S., Hirst P., 2010, MNRAS, 404, 629
Fanaroff B. L., Riley J. M., 1974, MNRAS, 167, 31
Fanti C. et al., 2004, A&A, 427, 465
Georganopoulos M., Kazanas D., 2004, ApJ, 604, L81
Hardcastle M. J. et al., 2016, MNRAS, 455, 3526
Lähteenmäki A., Valtaoja E., 1999, AJ, 117, 1168
Laing R. A., 1980, MNRAS, 193, 439
Leahy J. P., Black A. R. S., Dennett-Thorpe J., Hardcastle M. J., Komissarov S., Perley R. A., Riley J. M., Scheuer P. A. G., 1997, MNRAS, 291, 20
Mack K.-H., Prieto M. A., Brunetti G., Orienti M., 2009, MNRAS, 392, 705
Meisenheimer K., Yates M. G., Röser H.-J., 1997, A&A, 325, 57
Nagai H. et al., 2016, ApJ, 824, 132
Orienti M., Prieto M. A., Brunetti G., Mack K.-H., Massaro F., Harris D., 2012, MNRAS, 419, 2338
Perlman E. S., Georganopoulos M., May E. M., Kazanas D., 2010, ApJ, 708, 1
Perucho M., Martí J.-M., Quilis V., Ricciardelli E., 2014, MNRAS, 445, 1462
Prieto M. A., Kotilainen J. K., 1997, ApJ, 491, 77
Prieto M. A., Brunetti G., Mack K.-H., 2002, Science, 298, 193
Tchekhovskoy A., Bromberg O., 2016, MNRAS, 461L, 46
Thomson R. C., Crane P., MacKay C. D., 1995, ApJ, 446, 93
Tingay S. J., Lenc E., Brunetti G., Bondi M., 2008, AJ, 136, 2473

This paper has been typeset from a TEX/LATEX file prepared by the author.